PAPER

Check for updates

Low-temperature access to active iron and iron/nickel nitrides as potential electrocatalysts for the oxygen evolution reaction

Christopher R. DeLaney,[a] Sergio Diaz-Abad,[b] Shamus O'Leary,[a] Anna Gonzàlez-Rosell,[a] Ulises Martinez,†[b] Sandip Maurya, [b] Sergei A. Ivanov [a] and John Watt [*a]

Low-temperature, scalable routes to transition metal nitride (TMN) nanoparticles are desirable for a wide range of applications, yet their synthesis typically requires high temperatures (>350 °C) and reactive gas environments (*e.g.*, NH_3 or H_2/N_2). Here, we report a colloidal synthesis of mono- and bimetallic TMN nanoparticles using preformed metal carbonyl clusters as precursors and urea or diethylenetriamine (DETA) as nitrogen sources. This strategy enables access to size-controlled, phase-pure ε-Fe_3N_x and $Fe_yNi_{3-y}N$ nanoparticles at temperatures below 300 °C, without the need for flowing reactive gas atmospheres. By systematically varying nitrogen precursor, reaction temperature, and cluster identity, we achieve tunable nitrogen stoichiometry (x) and phase selectivity between N-rich and N-poor TMNs. Structural and magnetic characterization confirms clean decomposition of the precursors and phase formation consistent with controlled nitridation at the nanoscale. Preliminary electrochemical measurements in alkaline media demonstrate that these materials exhibit oxygen evolution reaction (OER) overpotentials comparable to RuO_2, highlighting their viability for future electrocatalytic applications.

1. Introduction

Hydrogen (H_2) has long been proposed as a solution to the climate crisis. However, significant challenges remain before it can effectively replace fossil fuels.[1,2] One of the main barriers to large-scale hydrogen utilization is the lack of efficient and cost-effective catalysts for the oxygen evolution reaction (OER), the corresponding half-reaction that complements the hydrogen evolution reaction (HER) in overall water splitting.[3–5] The OER suffers from sluggish kinetics due to the high overpotential required to drive the reaction. This is primarily caused by a scaling relationship between the binding energies of two critical OER intermediates, *OH and *OOH, which limits the ability to optimize both simultaneously.[6] Therefore, identifying catalysts that can break this relationship and effectively lower OER overpotential is critical, as the current industry-standard OER catalysts, iridium oxide (IrO_2) and ruthenium oxide (RuO_2), both suffer from high cost and limited supply.[7] This has driven the search for catalysts composed of earth-abundant

elements,[8] with first-row transition metals such as Fe, Co, and Ni emerging as promising alternatives.[9–12] These base metals along with their oxides,[13–15] phosphides,[16] carbides,[17–23] and nitrides[9,12] have recently attracted significant research interest. Among these, transition metal nitrides (TMNs) are particularly promising candidates due to their electronic structure, which resembles Pt or Pd near the Fermi level, as well as their high electrical conductivity and resistance to oxidation and corrosion.[18,24–26] Iron nitrides, in particular, are attractive because iron is the most cost-effective transition metal. However, the complex Fe–N phase diagram presents challenges in synthesizing well-defined, single-phase materials at the nanoscale.[27]

Synthesis of TMNs typically occurs under a flow of NH_3 or H_2/N_2 gas at high temperatures (>500 °C) and pressures to drive nitrogen to interstitial sites of the metal lattice, often with the use of a carbon-based support.[28–34] Li *et al.* synthesized Fe/Fe₃N NPs in solution at 260 °C but required a further annealing step at 525 °C to isolate ε-Fe_3N.[35] Such harsh reaction conditions and high temperatures complicate phase control and often yield mixed-phase products. In addition, these conditions also hinder precise control over nanoparticle morphology and size.

Despite these challenges, several TMNs have exhibited promising performance as oxygen evolution reaction (OER) catalysts. For example Fe_4N/Fe_3N supported by carbon nanotubes synthesized by Cui *et al.* demonstrated a low overpotential of 121 mV and Fe_4N/Fe_3N films supported on a graphene/nickel

[a] Center for Integrated Nanotechnologies, Materials Physics and Applications Division, Los Alamos National Laboratory, Los Alamos, New Mexico 87545, USA. E-mail: watt@lanl.gov

[b] Materials Synthesis and Integrated Devices, Materials Physics and Applications Division, Los Alamos National Laboratory, Los Alamos, New Mexico 87545, USA

† Current address: Sandia National Laboratories, Albuquerque, New Mexico 87185, USA.

This journal is © The Royal Society of Chemistry 2025

J. Mater. Chem. A, 2025, **13**, 40105–40113 | **40105**

foam synthesized by Yu *et al.* displayed a small Tafel slope 44.5 mV dec^{-1}, both of which are key indicators of high catalytic efficiency.[29,33]

Although monometallic TMNs have shown great efficacy as OER catalysts, bimetallic TMNs offer even greater potential. The presence of two distinct metal sites can stabilize OER intermediates more effectively, which has led to more promising overpotentials when compared to monometallic counterparts. For instance, bimetallic Ni$_3$FeN nanoparticles have been produced through NH$_3$ nitridation of NiFe precursors at high temperatures (*e.g.*, 500–700 °C), achieving OER overpotentials between 220–280 mV and Tafel slopes as low as 41 mV dec^{-1}.[36–40] Wang *et al.* produced OER-active Ni$_3$FeN from K$_3$[Fe(CN)$_6$]/Ni(OH)$_2$ upon heating the mixture at 380 °C for two hours under an atmosphere of NH$_3$, and showed a high activity for the OER in alkaline medium with a low overpotential of 200 mV at 10 mA cm^{-2} and a Tafel slope of 36 mV dec^{-1}.[41] These metrics surpass many monometallic TMNs, underlining the promise of bimetallic systems despite the synthetic complexity involved.

In this work, we report a low-temperature colloidal synthesis of catalytically active monometallic iron nitride and bimetallic iron–nickel nitride nanoparticles, using preformed metal carbonyl clusters as precursors.[42] Building on the known ability of carbonyl clusters to decompose cleanly, we use them to synthesize TMN nanoparticles below 300 °C without the use of NH$_3$.[43] By varying the nitrogen source and starting cluster, we access both N-rich and N-poor ε-Fe$_3$N$_x$ NPs, as well as bimetallic Fe$_y$Ni$_{3-y}$N NPs. The resulting TMN NPs demonstrate promising OER catalytic performance, comparable to the industrial standard noble metal oxide, RuO$_2$. Although these materials show promising OER activity, our focus here is on understanding synthetic parameters that govern phase purity and nitrogen incorporation. The current synthesis strategy, based on inexpensive transition metals, mild conditions, and controlled precursor chemistry, therefore offers a scalable and cost-effective route for developing next-generation OER catalysts.

2. Results and discussion

2.1. Synthesis and characterization of Fe$_3$N$_x$ phases

The most common methods for synthesizing TMN NPs involve a nitridation step carried out at high temperatures under high-pressure flow of N$_2$ or NH$_3$. This requirement has limited the applicability of established size-, shape-, and compositional-control strategies that have been effective in synthesizing other classes of NPs.[2,44] Here, we introduce a low-temperature colloidal synthesis approach using urea as the nitrogen source. Urea was selected for its low cost, ease of handling, and higher reactivity compared to molecular N$_2$ and NH$_3$.[45] For introduction into the reaction, urea is first dissolved in a polar high-boiling-point solvent, dimethylformamide (DMF), and then combined with a metal carbonyl cluster precursor (M$_x$(CO)$_y$). This precursor mixture is subsequently added dropwise into a flask containing another high-boiling-point solvent. Controlled and continuous addition in this manner has previously been demonstrated to afford excellent size control during the growth of high-quality iron oxide NPs.[2]

We initially focused on the use of preformed metal carbonyl clusters to synthesize monometallic iron nitride NPs, specifically ε-Fe$_3$N$_x$. This phase typically crystallizes in the $P6_322$ space group, featuring hexagonally close-packed (hcp) iron atoms with interstitial nitrogen partially occupying a subset of available octahedral sites. However, due to the multiple structurally equivalent interstitial sites and the variable nitrogen occupancy, the Fe–N phase diagram exhibits a substantial region of non-stoichiometry. As the nitrogen content increases from $x = 0.60$ to 1, nitrogen atoms preferentially occupy the well-ordered octahedral sites (N$_{2b}$ and N$_{2c}$), as depicted in Scheme 1.[46,47] When x exceeds 1, these ordered sites become saturated and excess N atoms begin to occupy the N$_{extra}$ positions. This occupancy leads to structural changes, with the space group transitioning from hexagonal $P6_322$ (for stoichiometric ε-Fe$_3$N) to trigonal $P3_12$ as more disordered N sites become populated. By carefully tuning both the stoichiometry of the metal carbonyl precursor and the availability of nitrogen during synthesis, we were able to selectively access from N-rich to N-poor ε-Fe$_3$N$_x$
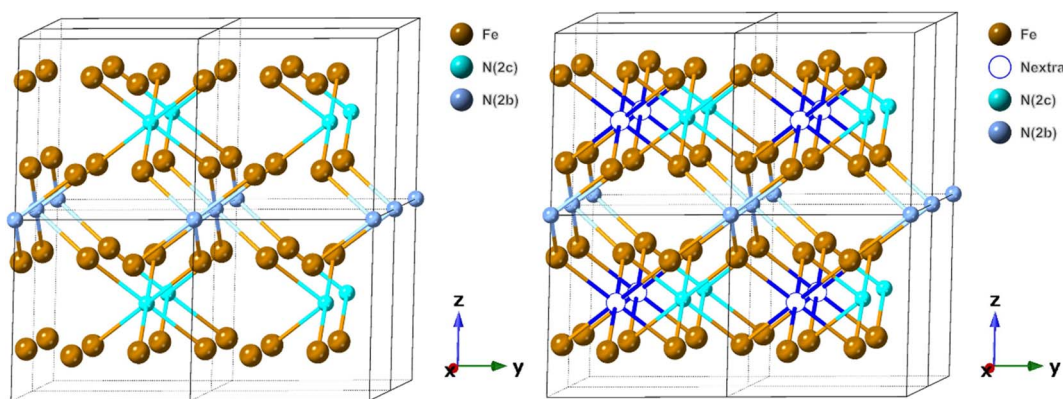
Scheme 1 Crystal structure of ε-Fe$_3$N$_x$. Three independent octahedral nitrogen positions are shown in dark blue (N$_{extra}$), cyan (N$_{2c}$), and light blue (N$_{2b}$). In fully stoichiometric Fe$_3$N, nitrogen is equally distributed among Fe atoms, occupying only the positions 2b and 2c. When $x > 1$, nitrogen disorder arises as additional N atoms occupy N$_{extra}$ sites, increasing nitrogen occupancy in alternating layers.

40106 | *J. Mater. Chem. A*, 2025, **13**, 40105–40113

This journal is © The Royal Society of Chemistry 2025

phases at nanoscale. Previous studies on late transition metal nitrides have demonstrated that catalytic performance is highly sensitive to nitride stoichiometry. Additionally, the magnetic properties of iron nitrides are also known to be extremely responsive to variations in nitrogen content, suggesting that even modest changes in x can produce significant changes in the material's physical and catalytic behaviors.[35,48,49]

2.1.1. Synthesis of ε-Fe$_3$N$_x$ NPs using Fe$_3$(CO)$_{12}$ as a cluster precursor. To produce monometallic iron nitride NPs, a precursor solution was prepared by first dissolving commercially available Fe$_3$(CO)$_{12}$ in 1.85 M urea in DMF (saturated solution), resulting in a 28:1 urea to Fe$_3$(CO)$_{12}$ ratio. The resulting deep red solution was subsequently added dropwise at 2 mL h^{-1} into a flask containing oleylamine (OLA) heated to 270 °C and kept under a flowing N$_2$ atmosphere. The mixture was held at 270 °C for an additional hour before being quenched and purified for analysis, with the results given in Fig. 1. The as-synthesized NPs were characterized by X-ray diffraction (XRD) (Fig. 1a) and matched closely with N-rich ε-Fe$_3$N$_{1.22}$ (PDF4+ card# 04-011-6419), which exists in the $P6_322$ space group with lattice spacings of $a = 4.74$ Å and $c = 4.40$ Å ($V_{cell} = 85.6$ Å^3). Transmission electron microscopy (TEM) images of the as-synthesized NPs are given in Fig. 1b. The NPs are measured to be 15.0 nm in size with a polydispersity of 2.1% (Fig. S1).

Accurately determining the nitrogen content in iron nitride nanoparticles is complicated by the broadening of XRD reflections and the limited sensitivity of individual diffraction peaks to small variations in nitrogen concentration in Fe$_3$N$_x$. As such, angular shifts of specific reflections cannot be used as a reliable indicator of nitrogen content. However, previous studies have shown that the unit cell volume obtained from Rietveld refinement scales linearly with x in bulk ε-Fe$_3$N$_x$ following the relation: V (Å^3) $= 10.637x + 72.858$.[50] Applying this equation to our data gives $x = 1.4$ in ε-Fe$_3$N$_x$ particles synthesized from Fe$_3$(CO)$_{12}$ and urea. The Curie temperature (T_C) of ε-Fe$_3$N$_x$ NPs can also provide insight into stoichiometry, as it is highly sensitive to the Fe:N ratio.[35,46] To complement the structural data, we used vibrating sample magnetometry (VSM) to estimate the composition. The magnetic moment (M) as a function of temperature (T) is shown in Fig. 1c. For the as-synthesized NPs, T_C was determined to be 480 K by differentiating the $M(T)$ curve and identifying the temperature corresponding to the minimum (see Fig. S2). Comparing this value to reported T_C vs. composition data (Fig. S3) yields a composition of ε-Fe$_3$N$_{1.08}$. The difference between x values derived from XRD and VSM likely reflect nanoscale effects that cause deviations from the bulk trend, including likely expected lattice expansion caused by high ionicity and surface curvature as well as the influence of uncompensated surface spins.[51] Because XRD tends to overestimate nitrogen content under these conditions, we adopt more conservative $x = 1.08$, as established from magnetic measurements, as the more accurate value. These results confirm that the use of Fe$_3$(CO)$_{12}$ as the iron source leads to the formation of nitrogen-rich TMN NPs.[46,52]

To explore the effect of nitrogen availability, we systematically varied the urea-to-iron ratio, as shown from XRD results presented in Fig. 2a. In the absence of urea, the resulting product consisted primarily of α-Fe and Fe$_3$O$_4$, with no detectable iron nitride phase. Although XRD cannot conclusively differentiate between some iron oxide phases at nanoscale (e.g., Fe$_3$O$_4$ and Fe$_2$O$_3$), the data clearly indicates oxidation when no nitrogen source is present. At a 6:1 urea:Fe$_3$(CO)$_{12}$ ratio, the ε-Fe$_3$N$_x$ (111) reflection appears, suggesting urea acts as an effective nitrogen donor, though metallic and oxidized iron phases remain. At 11:1 and 17:1 ratios, ε-Fe$_3$N$_x$ becomes the dominant phase, and by 28:1, only ε-Fe$_3$N$_{1.08}$ phase is observed, with no remaining reflections from α-Fe or iron oxides. The (111) reflection also shifts from 43.4° to 42.9°, consistent with progressive nitrogen incorporation and a final composition of $x = 1.08$, mirroring previous observations in similar systems.[35]

Reaction temperature similarly governs phase development as shown in Fig. 2b. At 230 °C, ε-Fe$_3$N$_x$ appears but coexists with α-Fe and iron oxide. At 250 °C, Fe$_3$N$_{1.08}$ dominates and at 270 °C it is the only detectable phase. The same shift in the (111) reflection of ε-Fe$_3$N$_x$ to lower angles is observed, again indicating nitrogen uptake. Interestingly, at 290 °C, α-Fe and iron oxide reappear, implying that above 270 °C, urea's fast decomposition causes it to lose its effectiveness as a nitrogen donor,
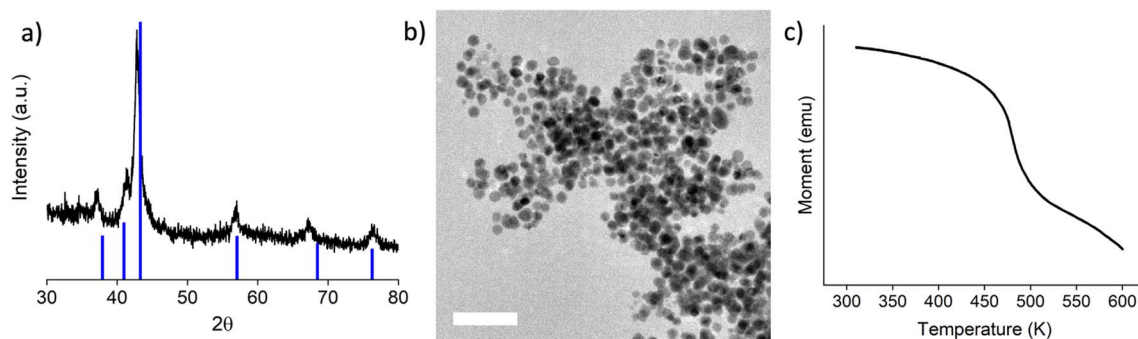
Fig. 1 (a) X-Ray diffraction (XRD) powder pattern of ε-Fe$_3$N$_{1.08}$ NPs produced from the low-temperature colloidal synthesis using Fe$_3$(CO)$_{12}$ as a cluster precursor, which matches closely with the reference pattern in blue from N-rich ε-Fe$_3$N$_{1.22}$ (PDF-4+ card# 04-011-6419). (b) Transmission electron microscopy (TEM) image of ε-Fe$_3$N$_{1.08}$ NPs. Scale bar = 100 nm. (c) VSM moment (M) versus temperature (T) plot of the as-synthesized NPs used to determine Curie temperature (T_C).
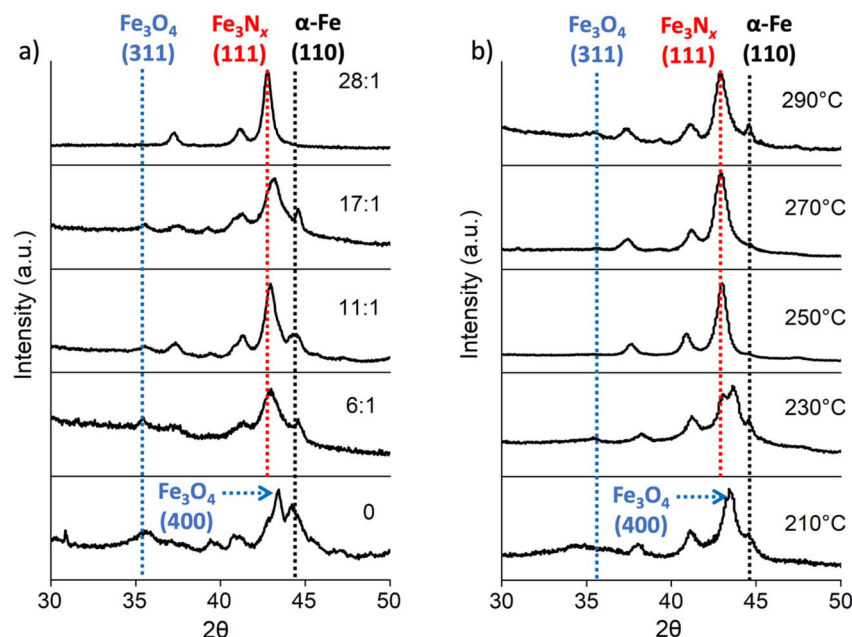
This journal is © The Royal Society of Chemistry 2025

J. Mater. Chem. A, 2025, **13**, 40105–40113 | **40107**

Fig. 2 XRD patterns of NPs prepared from $Fe_3(CO)_{12}$ with (a) increasing concentration of urea and (b) varying reaction temperature. The (111) reflection of ε-Fe_3N_x is marked in red, while the (311) of magnetite (Fe_3O_4) and (110) reflection of α-Fe are shown in green and black, respectively. The (400) reflection of Fe_3O_4, observed at low urea concentration and temperature, is also labeled. Panel (a) reflects that increasing the relative amount of urea causes the (111) reflection of ε-Fe_3N_x to emerge and shift to lower angles, signaling enhanced nitrogen incorporation. Similar trend is evident in panel (b) with increasing temperature.

leading to incomplete nitridation and the formation of undesirable byproducts. The consistent formation of ε-$Fe_3N_{1.08}$ at intermediate temperatures and sufficient urea loading suggest this phase is thermodynamically favored under the given conditions.

Since both OLA and DMF contain nitrogen, we assessed wheather they could contribute to nitridation in the absence of urea. In each case, precursor solutions were added dropwise into a hot solvent at 270 °C under N_2, followed by an additional hour of annealing. Using OLA as the reaction solvent and DMF for dissolution of the iron cluster resulted in only trace of ε-Fe_3N_x with most of the product composed of α-Fe and iron oxide (Fig. S4a). Substituting OLA with octadecene (ODE), a high-boiling-point hydrocarbon, produced nearly identical outcome (Fig. S4b). Using OLA as both the reaction and cluster solvent, yielded no nitridation (Fig. S4c), and neither did the combination of OLA and ODE (Fig. S4d). These results clearly show that OLA does not act as a nitrogen source under the reaction conditions tested. In contrast, DMF does appear to release some nitrogen, but only to a very limited extent.

To mitigate oxygen contamination from DMF and urea, and potentially increase the available nitrogen, we also explored the use of diethylenetriamine (DETA) as an alternative nitrogen donor. DETA is known to form nitrogen-rich coordination complexes and has a relatively high boiling point (207 °C). While its use has previously been demonstrated in forming iron nitride phases from $FeCl_3$ at much higher (560 °C) temperatures,[53] we tested it under our lower-temperature conditions. Dropwise addition of $Fe_3(CO)_{12}$ in DETA into hot OLA at 270 °C produced largely (70%) ε-Fe_3N_x with a minor α-Fe component

(<30%) according to XRD (Fig. S4e). Substituting OLA with ODE gave nearly identical results (Fig. S4f). These findings suggest that although DMF provides some nitrogen, both urea and polyamines such as DETA are significantly more effective nitrogen donors when used with $Fe_3(CO)_{12}$.

2.1.2. Synthesis of Fe_3N_x NPs using anionic $[Fe_4N(CO)_{12}]^-$ cluster precursor. To explore the versatility of the newly developed low-temperature colloidal synthesis, we aimed to increase the iron-to-nitrogen ratio toward Fe_4N_x. The initial experiments using the triiron cluster precursor consistently yielded ε-$Fe_3N_{1.08}$ as the thermodynamically favored phase. This suggests that a precursor with a higher iron content might promote a greater iron content in the resulting NPs. To test this, we employed nitrogen-containing iron carbonyl cluster $[Fe_4N(CO)_{12}]^-$, a close analogue of $Fe_3(CO)_{12}$. Previous studies reported that chemical vapor deposition of $HFe_4N(CO)_{12}$ at 200 °C resulted in a mixed γ'-Fe_4N/Fe thin film.[54] This cluster, available with either Et_4N^+ or H^+ counter ions, incorporates a Fe_4 metal center and pre-incorporated nitrogen. The nitrogen is believed to serve a dual role: stabilizing the four-metal center and facilitating nitride formation. The air-stable (NEt_4) $[Fe_4N(CO)_{12}]$ was synthesized in high yield *via* a known procedure, then it was protonated with H_3PO_4 to yield $HFe_4N(CO)_{12}$.[55,56] Both species were evaluated as precursors for TMN NP formation.

The synthetic procedure closely mirrored that used for $Fe_3(CO)_{12}$: the cluster was dissolved in a saturated DMF solution of urea (urea-to-cluster ratio of 28 : 1), and this solution was added dropwise over 1 hour to hot OLA (at 270 °C), followed by an additional hour of reaction. The resulting NPs were analyzed
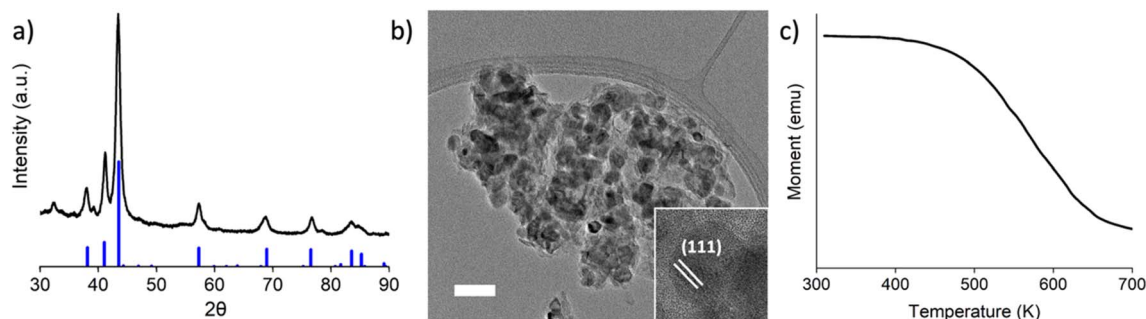
40108 | *J. Mater. Chem. A*, 2025, **13**, 40105–40113

This journal is © The Royal Society of Chemistry 2025

Fig. 3 (a) Powder XRD pattern of ε-Fe$_3$N$_{0.93}$ NPs produced using (NEt$_4$)[Fe$_4$N(CO)$_{12}$] in a low-temperature colloidal synthesis, shows close agreement with the reference ε-Fe$_3$N pattern (PDF-4+ card# 04-007-3379, in blue). (b) TEM image of as-synthesized ε-Fe$_3$N$_{0.93}$ NPs. Scale bar: 50 nm. (c) VSM magnetization (M) versus temperature (T) plot of the as-synthesized NPs.

via XRD (Fig. 3a), producing a pattern matching ε-Fe$_3$N (PDF-4+ card# 04-007-3379) with the $P6_322$ space group and a lattice spacing of $a = 4.69$ Å and $c = 4.36$ Å. The refined unit cell volume, 83.05 Å^3, corresponds to Fe$_3$N$_{0.96}$. TEM images of the as-synthesized NPs (Fig. 3b) showed spherical NPs with an average diameter of 16.6 nm and 4.9% polydispersity (Fig. S5), often displaying a flake-like attachment. High-resolution TEM (inset) revealed lattice fringes with 2.1 Å spacing, consistent with the (111) planes of ε-Fe$_3$N. The Curie temperature (T_C), derived from the derivative of the M–T curve (Fig. S6), was 598 K. These values are slightly higher than the 575 K reported for stoichiometric ε-Fe$_3$N, indicating a sub-stoichiometric nitrogen content consistent with ε-Fe$_3$N$_{0.93}$ (Fig. S3).[35] Per our discussion above, due to the deviations at nanoscale, we refer to these NPs as ε-Fe$_3$N$_{0.93}$.

Similarly to case of Fe$_3$(CO)$_{12}$, the reaction with (NEt$_4$) [Fe$_4$N(CO)$_{12}$] was sensitive to urea concentration (Fig. 4a). As the urea-to-cluster ratio increased from 0:1 to 28:1, so did nitrogen incorporation in ε-Fe$_3$N$_x$. Without urea, iron oxide and α-Fe dominated the product. At 28:1, ε-Fe$_3$N$_{0.93}$ was the primary phase (>97%) with only minor iron oxide and α-Fe impurities. Notably, unlike reactions with Fe$_3$(CO)$_{12}$, increasing urea concentration did not cause the XRD peak to shift toward 42.9° but rather maintained it near 43.4°, supporting the assignment of more nitrogent-deficient ε-Fe$_3$N$_{0.93}$ phase.

Temperature also played a critical role (Fig. 4b). At temperatures below 250 °C, minimal ε-Fe$_3$N$_x$ formed; at 270 °C, ε-Fe$_3$N$_x$ became the dominant phase. Above 270 °C, the formation of α-Fe and iron oxide increased, consistent with the side reactions due to excessive urea decomposition. Compared to Fe$_3$(CO)$_{12}$,
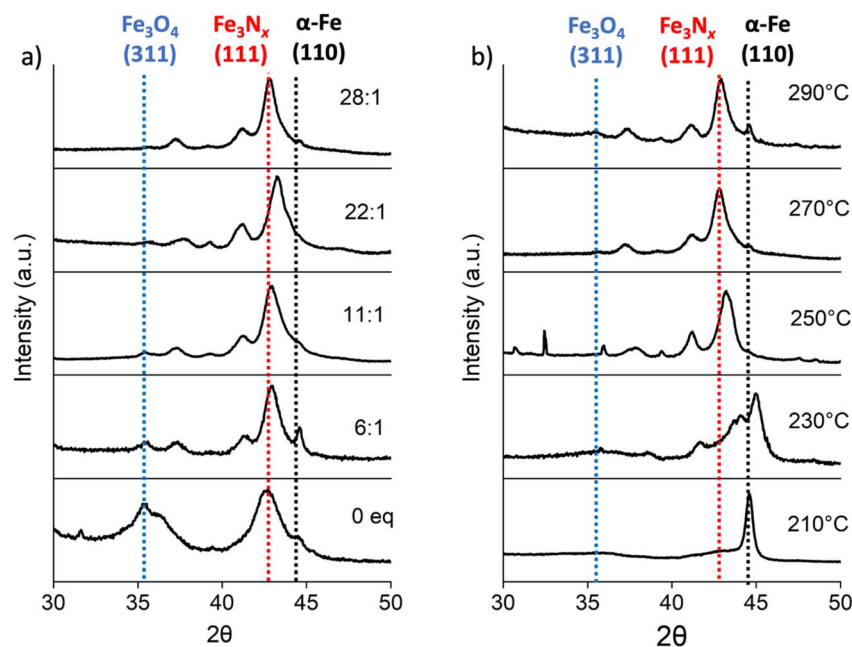

Fig. 4 Powder XRD patterns of nanoparticles obtained from (NEt$_4$)[Fe$_4$N(CO)$_{12}$] showing (a) effects of urea concentration and (b) effects of temperature. The reference lines: ε-Fe$_3$N (111) in red, α-Fe (110) in black, and iron oxide (311) in blue. The increase in (a) the relative proportion of urea or (b) the reaction temperature shifts primary phase from α-Fe and iron oxide to ε-Fe$_3$N.

This journal is © The Royal Society of Chemistry 2025

J. Mater. Chem. A, 2025, **13**, 40105–40113 | **40109**

the optimal temperature window for $Fe_4N(CO)_{12}$-based synthesis was narrower. This is possibly due to its better solubility in the DMF/urea mixture and more rapid CO ligand displacement. Assuming complete substitution of CO with urea, the hypothetical Fe : N ratio in $[Fe_4N(Urea)_{12}]^-$ is 4 : 13 versus 3 : 12 for $Fe_3(CO)_{12}$ – derived species. This could explain the lower nitrogen content in the resulting NPs from the $[Fe_4N(CO)_{12}]^-$ route. These findings confirm that 270 °C is the optimal temperature for ε-Fe_3N_x formation, regardless of the iron cluster used. Moreover, they suggest that urea is the main nitrogen source; the nitrogen pre-incorporated in the cluster likely leaves the reaction prior to contributing to the final nitride structure. Its main function appears to be stabilizing the Fe_4 core and enhancing the iron content of the resulting NPs. At 270 °C, decomposition of both iron cluster and urea appears synchronized, maximizing TMN formation while minimizing side reactions. Lower temperatures suppress nitridation, leading to metallic iron, while higher temperatures accelerate urea decomposition and competing oxidation.

The protonated cluster $HFe_4N(CO)_{12}$ behaves similarly. Dropwise addition of a 28 : 1 urea-to-cluster solution in DMF to OLA at 200 °C (a CVD condition for γ'-Fe_4N/Fe thin films) yielded predominantly α-Fe/iron oxide with a minor ε-Fe_3N_x component (Fig. S7). Increasing temperature to 270 °C produced ε-Fe_3N_x (Fig. S8), consistent with previous cases and nearly identical with the anionic cluster results. As mentioned previously, substituting DMF/urea with DETA (a potential nitrogen donor) in reactions with either cluster also produced ε-Fe_3N_x at 270 °C (Fig. S9 and S10), demonstrating that DETA is a viable N-donor across various iron-carbonyl clusters.

2.2. Synthesis and characterization of bimetallic $Fe_yNi_{3-y}N$

Bimetallic TMN NPs have recently demonstrated improved catalytic activity in water splitting reactions, attributed to synergistic effects between two metal centers in close proximity.[38,57,58] Fe favors adsorption of OH* and O*, while Ni better stabilizes OOH*, enabling a dual-site mechanism with parallel pathways, lowering energy barriers and making the bimetallic catalyst more effective than either metal alone.[59,60] Motivated by this, we explored Ni incorporation into the TMN NPs, as Ni is the next least expensive early transition metal after Fe. Previous

work by Della Pergola et al. showed that a reaction between $(NEt_4)_2[Ni_6(CO)_{12}]$ and $(NEt_4)[Fe_4N(CO)_{12}]$ in MeCN produced bimetallic clusters with the general formula $(NEt_4)_x[Fe_6Ni_6N_2(CO)_{24}]$.[61] As such, the $(NEt_4)_2[Ni_6(CO)_{12}]$ cluster was selected as a potential additional precursor for the formation of bimetallic TMN NPs. A 1 : 2 mixture of $(NEt_4)_2[Ni_6(CO)_{12}]$ and $[NEt_4][Fe_4N(CO)_{12}]$ was stirred in acetonitrile for 72 hours to yield a dark brown solution, which was then dried. The resulting solid was extracted into 4.5 mL of DETA and added dropwise into 12 mL of OLA at 290 °C over the course of one hour, followed by an additional one hour of incubation. We found that effective formation of a bimetallic phase required a higher reaction temperature (290 °C) than what was previously optimal for ε-Fe_3N_x NPs (270 °C). However, as shown in Fig. 2b, preforming a reaction at 290 °C in a urea/DMF mixture led to the formation of unwanted side products, an outcome that was also encountered here (Fig. S11). Accordingly, DETA was selected as the nitrogen source, as it remains effective at higher reaction temperatures.

The diffraction pattern of the resulting product matches well with $Fe_{0.73}Ni_{0.27}N_{0.33}$ (PDF-4+ card# 04-014-1599), which has a hexagonal structure (space group of $P6_3/mmc$) and lattice spacings of $a = 2.378$ Å and $c = 4.382$ Å (Fig. 5a). A slight shift to higher angles was observed for the higher-index reflections. The Fe : Ni ratio was determined by ICP-OES to be 1.82 : 1, consistent with X-Ray energy-dispersive spectroscopy (XEDS) (Fig. S12), indicating the formation of $Fe_{1.94}Ni_{1.06}N$ TMN NPs. A higher Ni content is expected to shift XRD peaks to higher 2θ values, further supporting proposed stoichiometry. TEM images (Fig. 5b) show that particles are small ($\sim$7 nm) but somewhat aggregated, complicating size distribution analysis. Magnetic measurements reveal a Curie temperature (T_C) of $\sim$450 K, lower than that of ε-Fe_3N_x, as expected due to incorporation of the less magnetic Ni (Fig. S13).

Substituting $(NEt_4)[Fe_4N(CO)_{12}]$ with commercial $Fe_3(CO)_{12}$ in the reaction with $(NMe_4)_2[Ni_6(CO)_{12}]$ did not lead to well-defined particles, whether using DMF/urea or DETA (Fig. S14 and 15). While the XRD pattern (Fig. S15) from DETA reaction appears consistent with a TMN phase, TEM images reveal poor crystallinity and dispersity (Fig. S16). Additionally, ICP-OES analysis of these particles shows a much higher iron content
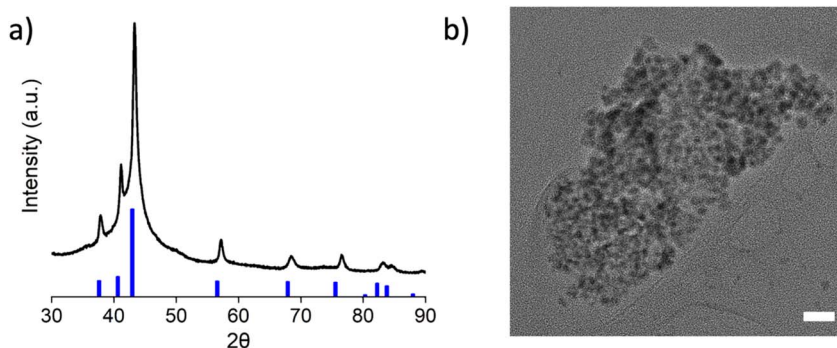

Fig. 5 (a) XRD powder pattern of the as-synthesized $Fe_{1.94}Ni_{1.06}N$ NPs from a low-temperature colloidal synthesis. (b) TEM image of the $Fe_{1.94}Ni_{1.06}N$ nanoparticles, scale bar of 25 nm.

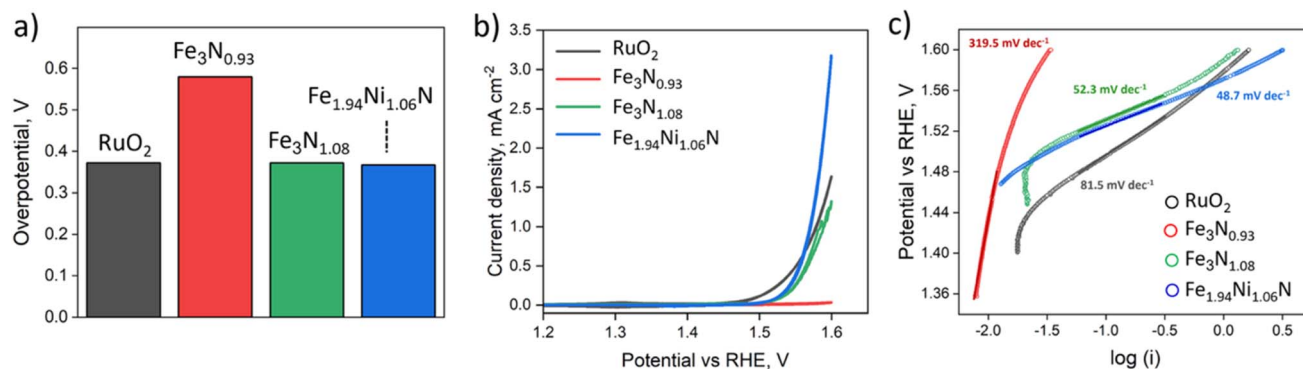**40110** | J. Mater. Chem. A, 2025, **13**, 40105–40113

This journal is © The Royal Society of Chemistry 2025

Fig. 6 (a) Overpotential at 10 mA cm^{-2} for RuO$_2$, and the TMN NPs; ε-Fe$_3$N$_{0.93}$, ε-Fe$_3$N$_{1.08}$, and Fe$_{1.94}$Ni$_{1.06}$N. (b) LSVs and (c) Tafel analysis for RuO$_2$ and the TMN NPs; ε-Fe$_3$N$_{0.93}$, ε-Fe$_3$N$_{1.08}$, and Fe$_{1.94}$Ni$_{1.06}$N. Electrode: 5 mm glassy carbon (GC) disk electrode spinning at 800 rpm; electrolyte: 1 M KOH.

(Fe : Ni = 4 : 1) compared to the samples prepared with (NEt$_4$)[Fe$_4$N(CO)$_{12}$]. These results indicate that Fe$_3$(CO)$_{12}$ does not generate a suitable precursor for the formation of pure Fe$_y$-Ni$_{3-y}$N under tested conditions. Taken together, the data underscore the importance of both metal precursor selection and nitrogen source compatibility to achieve balanced decomposition kinetics when targeting TMN NPs *via* colloidal routes.

2.3. OER catalysis

The OER activities of the as-synthesized mono- and bimetallic TMN NPs underwent preliminary evaluation using linear sweep voltammetry (LSV) on a 5 mm glassy carbon (GC) disk electrode rotating at 800 rpm and were compared with industry-standard RuO$_2$ under identical experimental conditions. No evidence of magnetic agglomeration of the nanoparticles was observed during the preparation of the catalytic ink. The results of catalytic testing are shown in Fig. 6a, where RuO$_2$, ε-Fe$_3$N$_{0.93}$, ε-Fe$_3$N$_{1.08}$, and Fe$_{1.94}$Ni$_{1.06}$N catalysts exhibit overpotentials for OER of 370, 580, 372, and 367 mV, respectively, in 1 M KOH at a current density (j) of 10 mA cm^{-2}. The reported overpotential for RuO$_2$ agrees well with the literature value of 358 mV.[5] The OER overpotential of Fe$_3$N$_{1.08}$ and bimetallic Fe$_{1.94}$Ni$_{1.06}$N closely match that of RuO$_2$, while the N-deficient ε-Fe$_3$N$_{0.93}$ exhibits considerably higher overpotential.

LSV and Tafel analyses are shown in Fig. 6b and c. The monometallic ε-Fe$_3$N$_{1.08}$ and bimetallic Fe$_{1.94}$Ni$_{1.06}$N samples exhibit similar OER onset potentials (Fig. 6b) in 1 M KOH, whereas ε-Fe$_3$N$_{0.93}$ displayed a delayed onset and lower current density. Tafel analysis (Fig. 6c and Table S1) indicates that the ε-Fe$_3$N$_{1.08}$ and Fe$_{1.94}$Ni$_{1.06}$N TMN nanoparticles exhibit Tafel slopes comparable to RuO$_2$ under identical conditions with Tafel slopes of 52.3 mV dec^{-1} and 48.7 mV dec^{-1}, respectively, compared to 81.5 mV dec^{-1} for RuO$_2$. In contrast, the N-deficient ε-Fe$_3$N$_{0.93}$ catalyst exhibits poor performance, with a Tafel slope of 319.5 mV dec^{-1}. This reduced activity may stem from modulation of the surface electron density, which could lead to an inadequate residence time for key intermediates in the multi-step OER pathway.[62] Preliminary stability testing (24 h) is given in Fig. S17, showing promising catalyst durability.

3. Conclusion

We report a low-temperature (<300 °C) colloidal synthesis of transition metal nitride (TMN) nanoparticles that avoids the use of high temperatures and NH$_3$ or H$_2$/N$_2$ gas environments, producing a smaller more size-controlled product than conventional approaches. Starting from preformed metal carbonyl clusters (M$_x$(CO)$_y$) as iron precursors, which decompose cleanly in the presence of urea as a nitrogen source, we demonstrate that matching decomposition kinetics of the metal and nitrogen precursors is critical to avoid side product formation and oxidation. Diethylenetriamine (DETA) could also serve as a nitrogen source, though its reactivity was found to be less effective than that of urea.

Using commercial Fe$_3$(CO)$_{12}$ results in N-rich ε-Fe$_3$N$_{1.08}$ nanoparticles, whereas employing the tetranuclear cluster (NEt$_4$)[Fe$_4$N(CO)$_{12}$] yields more N-deficient ε-Fe$_3$N$_{0.93}$ product. In this case, the urea provides the bulk of nitrogen content, while the structural nitride in the cluster appears to stabilize the cluster core. Co-decomposition of iron and nickel carbonyl clusters in the presence of DETA leads to bimetallic Fe$_{1.94}$Ni$_{1.06}$N nanoparticles, with DETA acting as an effective nitrogen donor at higher temperatures than urea due to the higher stability of the former. All mono- and bimetallic TMNs produced in this work function as active electrocatalysts for water splitting, with particular efficiency in driving the sluggish oxygen evolution reaction (OER). Both N-rich and bimetallic compositions demonstrated OER activity within the expected range for TMNs under alkaline conditions, with OER overpotentials comparable to the benchmark RuO$_2$ catalyst. These promising preliminary electrocatalytic results, combined with the demonstrated tunability of nitrides and bimetallic systems, highlight the strong potential of our synthetic approach for further scale-up investigations and full-cell catalytic validation.

Conflicts of interest

The authors declare no competing financial interests.

This journal is © The Royal Society of Chemistry 2025

J. Mater. Chem. A, 2025, **13**, 40105–40113 | **40111**

Data availability

Experimental methods and additional experimental data supporting the findings of this article are available in the supplementary information (SI). See DOI: https://doi.org/10.1039/d5ta06347g.

Acknowledgements

References

1 N. S. Lewis and D. G. Nocera, *Proc. Natl. Acad. Sci. U. S. A.*, 2006, **103**, 15729–15735.

2 E. C. Vreeland, J. Watt, G. B. Schober, B. G. Hance, M. J. Austin, A. D. Price, B. D. Fellows, T. C. Monson, N. S. Hudak, L. Maldonado-Camargo, A. C. Bohorquez, C. Rinaldi and D. L. Huber, *Chem. Mater.*, 2015, **27**, 6059–6066.

3 J. Song, C. Wei, Z. F. Huang, C. Liu, L. Zeng, X. Wang and Z. J. Xu, *Chem. Soc. Rev.*, 2020, **49**, 2196–2214.

4 L. Yu, S. W. Song, B. McElhenny, F. Z. Ding, D. Luo, Y. Yu, S. Chen and Z. F. Ren, *J. Mater. Chem. A*, 2019, **7**, 19728–19732.

5 N. T. Suen, S. F. Hung, Q. Quan, N. Zhang, Y. J. Xu and H. M. Chen, *Chem. Soc. Rev.*, 2017, **46**, 337–365.

6 Z. W. Seh, J. Kibsgaard, C. F. Dickens, I. Chorkendorff, J. K. Norskov and T. F. Jaramillo, *Science*, 2017, **355**, eaad4998.

7 T. Reier, M. Oezaslan and P. Strasser, *ACS Catal.*, 2012, **2**, 1765–1772.

8 I. Roger, M. A. Shipman and M. D. Symes, *Nat. Rev. Chem.*, 2017, **1**, 0003.

9 N. Han, P. Liu, J. Jiang, L. Ai, Z. Shao and S. Liu, *J. Mater. Chem. A*, 2018, **6**, 19912–19933.

10 A. B. Dongil, *Nanomaterials*, 2019, **9**, 1111.

11 F. Lyu, Q. Wang, S. M. Choi and Y. Yin, *Small*, 2019, **15**, e1804201.

12 X. Peng, C. R. Pi, X. M. Zhang, S. Li, K. F. Huo and P. K. Chu, *Sustainable Energy Fuels*, 2019, **3**, 366–381.

13 F. Song, L. Bai, A. Moysiadou, S. Lee, C. Hu, L. Liardet and X. Hu, *J. Am. Chem. Soc.*, 2018, **140**, 7748–7759.

14 B. Zhang, X. Zheng, O. Voznyy, R. Comin, M. Bajdich, M. Garcia-Melchor, L. Han, J. Xu, M. Liu, L. Zheng, F. P. Garcia de Arquer, C. T. Dinh, F. Fan, M. Yuan, E. Yassitepe, N. Chen, T. Regier, P. Liu, Y. Li, P. De Luna, A. Janmohamed, H. L. Xin, H. Yang, A. Vojvodic and E. H. Sargent, *Science*, 2016, **352**, 333–337.

15 B. Zhang, L. Wang, Z. Cao, S. M. Kozlov, F. P. García de Arquer, C. T. Dinh, J. Li, Z. Wang, X. Zheng, L. Zhang, Y. Wen, O. Voznyy, R. Comin, P. De Luna, T. Regier, W. Bi, E. E. Alp, C.-W. Pao, L. Zheng, Y. Hu, Y. Ji, Y. Li, Y. Zhang, L. Cavallo, H. Peng and E. H. Sargent, *Nat. Catal.*, 2020, **3**, 985–992.

16 J. F. Callejas, C. G. Read, C. W. Roske, N. S. Lewis and R. E. Schaak, *Chem. Mater.*, 2016, **28**, 6017–6044.

17 C. Giordano, C. Erpen, W. Yao, B. Milke and M. Antonietti, *Chem. Mater.*, 2009, **21**, 5136–5144.

18 D. J. Ham and J. S. Lee, *Energies*, 2009, **2**, 873–899.

19 W. Yao, P. Makowski, C. Giordano and F. Goettmann, *Chemistry*, 2009, **15**, 11999–12004.

20 C. Giordano and M. Antonietti, *Nano Today*, 2011, **6**, 366–380.

21 C. Giordano and T. Corbiere, *Colloid Polym. Sci.*, 2012, **291**, 1297–1311.

22 Y. Hu, J. O. Jensen, W. Zhang, L. N. Cleemann, W. Xing, N. J. Bjerrum and Q. Li, *Angew Chem. Int. Ed. Engl.*, 2014, **53**, 3675–3679.

23 L. Fan, P. F. Liu, X. Yan, L. Gu, Z. Z. Yang, H. G. Yang, S. Qiu and X. Yao, *Nat. Commun.*, 2016, **7**, 10667.

24 M. Nagai, *Appl. Catal., A*, 2007, **322**, 178–190.

25 Y. Zhong, X. Xia, F. Shi, J. Zhan, J. Tu and H. J. Fan, *Adv. Sci.*, 2016, **3**, 1500286.

26 H. Wang, J. Li, K. Li, Y. Lin, J. Chen, L. Gao, V. Nicolosi, X. Xiao and J. M. Lee, *Chem. Soc. Rev.*, 2021, **50**, 1354–1390.

27 T. C. Monson, B. Zheng, R. E. Delaney, C. J. Pearce, Y. Zhou, S. Atcitty and E. Lavernia, *J. Mater. Res.*, 2021, **37**, 380–389.

28 L. Yu, S. W. Song, B. McElhenny, F. Z. Ding, D. Luo, Y. Yu, S. Chen and Z. F. Ren, *J. Mater. Chem. A*, 2019, **7**, 19728–19732.

29 F. Yu, H. Zhou, Z. Zhu, J. Sun, R. He, J. Bao, S. Chen and Z. Ren, *ACS Catal.*, 2017, **7**, 2052–2057.

30 Y. Hu, D. Huang, J. Zhang, Y. Huang, M. S. J. T. Balogun and Y. Tong, *ChemCatChem*, 2019, **11**, 6051–6060.

31 D. Liang, H. Zhang, X. Ma, S. Liu, J. Mao, H. Fang, J. Yu, Z. Guo and T. Huang, *Mater. Today Energy*, 2020, **17**, 100433.

32 W. Wang, L. Liu, W. C. Leng, L. L. Cui and Y. Gong, *Inorg. Chem.*, 2021, **60**, 12136–12150.

33 L. L. Cui, W. C. Leng, X. Liu and Y. Gong, *Nanotechnology*, 2022, **33**, 465402.

34 L. Kumaresan, G. Shanmugavelayutham and P. Saravanan, *Appl. Phys. A*, 2022, **128**, 1073.

35 Y. Li, D. Pan, Y. Zhou, Q. Kuang, C. Wang, B. Li, B. Zhang, J. Park, D. Li, C. Choi and Z. Zhang, *Nanoscale*, 2020, **12**, 10834–10841.

36 P. Li, Z. Jin, Y. Qian, Z. Fang, D. Xiao and G. Yu, *ACS Energy Lett.*, 2019, **4**, 1793–1802.

40112 | *J. Mater. Chem. A*, 2025, **13**, 40105–40113

This journal is © The Royal Society of Chemistry 2025

37 M. Chen, D. Liu, B. Zi, Y. Chen, D. Liu, X. Du, F. Li, P. Zhou, Y. Ke, J. Li, K. H. Lo, C. T. Kwok, W. F. Ip, S. Chen, S. Wang, Q. Liu and H. Pan, *J. Energy Chem.*, 2022, **65**, 405–414.

38 J. Jiang, X. L. Zhou, H. G. Lv, H. Q. Yu and Y. Yu, *Adv. Funct. Mater.*, 2022, **33**, 2212160.

39 X. D. Jia, Y. F. Zhao, G. B. Chen, L. Shang, R. Shi, X. F. Kang, G. I. N. Waterhouse, L. Z. Wu, C. H. Tung and T. R. Zhang, *Adv. Energy Mater.*, 2016, **6**, 1502585.

40 Y. Gu, S. Chen, J. Ren, Y. A. Jia, C. Chen, S. Komarneni, D. Yang and X. Yao, *ACS Nano*, 2018, **12**, 245–253.

41 J. Wang, F. Cao, C. Shen, G. Li, X. Li, X. Yang, S. Li and G. Qin, *Catal. Sci. Technol.*, 2020, **10**, 4458–4466.

42 S. Zacchini, *Eur. J. Inorg. Chem.*, 2011, 4125–4145, DOI: **10.1002/ejic.201100462**.

43 J. Watt, G. C. Bleier, M. J. Austin, S. A. Ivanov and D. L. Huber, *Nanoscale*, 2017, **9**, 6632–6637.

44 S. Cheong, J. D. Watt and R. D. Tilley, *Nanoscale*, 2010, **2**, 2045–2053.

45 T. Nakamura, H. Hayashi and T. Ebina, *J. Nanopart. Res.*, 2014, **16**, 2699.

46 H. A. Wriedt, N. A. Gokcen and R. H. Nafziger, *Bull. Alloy Phase Diagrams*, 1987, **8**, 355–377.

47 A. Leineweber, H. Jacobs, F. Hüning, H. Lueken, H. Schilder and W. Kockelmann, *J. Alloys Compd.*, 1999, **288**, 79–87.

48 M. Kodera and K. Sayama, *ChemCatChem*, 2022, **14**, e202201004.

49 S.-H. Baek, K. Yun, D.-C. Kang, H. An, M. B. Park, C.-H. Shin and H.-K. Min, *Catalysts*, 2021, **11**, 192.

50 K. D. Litasov, A. Shatskiy, D. S. Ponomarev and P. N. Gavryushkin, *J. Geophys. Res.:Solid Earth*, 2017, **122**, 3574–3584.

51 V. Perebeinos, S.-W. Chan and F. Zhang, *Solid State Commun.*, 2002, **123**, 295–297.

52 K. H. Jack, *Acta Crystallogr.*, 1952, **5**, 404–411.

53 W. Yin, D. Zhang, P. Zhang, X. Wang, W. Wang, X. Lei, Z. Shi and H. Yang, *J. Alloys Compd.*, 2016, **688**, 828–832.

54 T. P. Fehlner, M. M. Amini, W. F. Stickle, O. A. Pringle, G. J. Long and F. P. Fehlner, *Chem. Mater.*, 2002, **2**, 263–268.

55 D. E. Fjare and W. L. Gladfelter, *Inorg. Chem.*, 2002, **20**, 3533–3539.

56 M. Tachikawa, J. Stein, E. L. Muetterties, R. G. Teller, M. A. Beno, E. Gebert and J. M. Williams, *J. Am. Chem. Soc.*, 2002, **102**, 6648–6649.

57 Y. Lu, Z. Li, Y. Xu, L. Tang, S. Xu, D. Li, J. Zhu and D. Jiang, *Chem. Eng. J.*, 2021, **411**, 128433.

58 A. M. Henning, J. Watt, P. J. Miedziak, S. Cheong, M. Santonastaso, M. Song, Y. Takeda, A. I. Kirkland, S. H. Taylor and R. D. Tilley, *Angew Chem. Int. Ed. Engl.*, 2013, **52**, 1477–1480.

59 H. Xiao, H. Shin and W. A. Goddard 3rd, *Proc. Natl. Acad. Sci. U. S. A.*, 2018, **115**, 5872–5877.

60 C. C. Wu, X. M. Zhang, Z. X. Xia, M. Shu, H. Q. Li, X. L. Xu, R. Si, A. I. Rykov, J. H. Wang, S. S. Yu, S. L. Wang and G. Q. Sun, *J. Mater. Chem. A*, 2019, **7**, 14001–14010.

61 R. Della Pergola, M. Bruschi, F. Fabrizi de Biani, A. Fumagalli, L. Garlaschelli, F. Laschi, M. Manassero, M. Sansoni and P. Zanello, *C. R. Chim.*, 2005, **8**, 1850–1855.

62 J. K. Norskov, T. Bligaard, J. Rossmeisl and C. H. Christensen, *Nat. Chem.*, 2009, **1**, 37–46.

This journal is © The Royal Society of Chemistry 2025

J. Mater. Chem. A, 2025, **13**, 40105–40113 | **40113**